THE JOURNAL OF PHYSICAL CHEMISTRY B
A JOURNAL OF THE AMERICAN CHEMICAL SOCIETY

pubs.acs.org/JPCB

Article

Controlling Degradation and Erosion of Polymer Networks: Insights from Mesoscale Modeling

Vaibhav Palkar and Olga Kuksenok*

Cite This: J. Phys. Chem. B 2022, 126, 336−346

Read Online

ACCESS | Metrics & More | Article Recommendations | Supporting Information

ABSTRACT: Understanding and controlling degradation of polymer networks on the mesoscale is critical for a range of applications. We utilize dissipative particle dynamics to capture photocontrolled degradation and erosion processes in hydrogels formed by end-linking of four-arm polyethylene glycol precursors. We demonstrate that the polydispersity and the fraction of broken-off fragments scale with the relative extent of reaction. The reverse gel point measured is close to the value predicted by the bond percolation theory on a diamond lattice. We characterize the erosion process via tracking the mass loss that accounts for the fragments remaining in contact with the percolated network. We quantify the dependence of the mass loss on the extent of reaction and on the properties of the film prior to degradation. These results elucidate the main features of degradation and erosion on the mesoscale and could provide guidelines for future design of degrading materials with dynamically controlled properties.

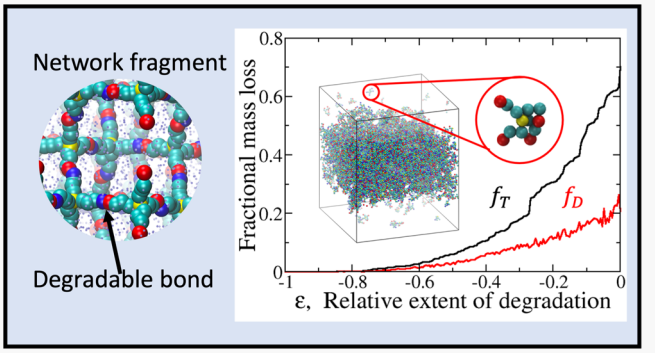

INTRODUCTION

Controlled degradation of polymer networks plays a vital role in a variety of applications ranging from the design of degradable thermoset polymers[1] to controlled delivery of drugs and biomolecules[2−4] and regulating growth of neural networks.[5] Of particular interest is photocontrolled degradation, which permits spatially resolved dynamic control of physical and chemical properties of the materials.[6−12] Notably, in a number of the above applications, either the characteristic features of degradable gels[5,6,8] or the dimensions of the entire degradable gel particle[4] range between nanometers to microns, the length scales referred to as mesoscopic. While analytical models and continuum approaches[13−19] inform our current understanding of hydrogel degradation, an understanding of degradation and erosion at the mesoscale to date is exceptionally limited despite the relevance of this length scale to a plethora of applications.

The term degradation commonly refers to the reaction that cleaves covalent bonds, while erosion refers to the mass loss that accompanies degradation.[13,18] Correspondingly, the polymer network undergoing degradation is often characterized by the mass loss capturing erosion processes,[1,13,20,21] and by the reverse gel point[1,13,14,20] capturing the critical extent of degradation reaction. Similar to the gel point, which is defined as a critical point of formation of an infinite percolating network during gelation,[22] the reverse gel point is a critical point corresponding to the disappearance of the percolating network.[1,13,20] This point is characterized by a critical value of the reaction conversion; the term reverse gel point is sometimes used interchangeably with gel point[13] when describing the degradation process. Notably, the disappearance of the percolating network at the reverse gel point results in a sudden drop in the mass of the polymer.[13,20]

To capture the polymer network degradation and erosion at the mesoscale, diffusion of all the network fragments along with reaction kinetics, hydrodynamic interactions, and network topology and heterogeneities need to be taken into account. We use dissipative particle dynamics (DPD)[23−25] to model these complex systems. DPD is a mesoscale approach utilizing soft repulsive interactions between the beads representing clusters of atoms; this approach has been widely used to model a variety of complex systems,[25−34] including dynamics of hydrogels in various environments.[35−44] To overcome unphysical topological crossings of bonded polymer chains, we recently adapted a modified segmental repulsive potential (mSRP) formulation[45] to model gels with degradable bonds.[46]

As a model system, we focus on hydrogels formed by the end-linking of four-arm polyethylene glycol (PEG) macromolecular precursors,[47−49] often referred to as tetra-PEG gels.[20,49,50] Tetra-PEG gels fabricated by Sakai et al.[49] have

Received: November 4, 2021
Revised: December 12, 2021
Published: December 29, 2021

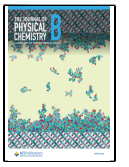

https://doi.org/10.1021/acs.jpcb.1c09570
J. Phys. Chem. B 2022, 126, 336−346

been shown to form nearly ideal network structures exhibiting superior mechanical properties prior to degradation. The near-ideality of the tetra-PEG gels is attributed to the elimination of a large fraction of defects during synthesis provided that the stoichiometric ratio of two macromonomer precursors is equal to one and that the overlap monomer concentration is used.[49] The four-arm PEG precursors can be modified during their synthesis to enable controlled degradation. Specifically, these hydrogels can be made degradable by including photocleavable functional groups, for example, the coumarin[47,51] and nitrobenzyl[10,51,52] groups, in the close vicinity of the end functionalities responsible for gelation.[47,51−53]

In what follows, we characterize the degradation process via tracking the time evolution of distribution of network fragments. We show that the reverse gel point can be reliably calculated from the reduced weight-average and z-average degrees of polymerization of network fragments. Based on the calculated reverse gel point, we define the relative extent of reaction and show that the polydispersity and the fraction of broken-off fragments scale with the relative extent of reaction for the samples with various thicknesses and crosslink densities. Furthermore, we characterize erosion from the swollen polymer network via tracking the apparent mass loss that accounts for the fragments remaining in contact with the percolated network. The proposed framework allows one to clearly distinguish the main features of degradation and erosion on the mesoscale.

METHODS

Dissipative Particle Dynamics. The main features of the DPD approach are briefly outlined below. More details on DPD methodology can be found in the original publications,[24,54,55] while latest developments are surveyed in the recent reviews.[25,56] The beads in DPD represent collection of atoms, and the motion of these beads is governed by the Newton's equations of motion[24]

$$\frac{\mathrm{d}\boldsymbol{r}_i}{\mathrm{d}t} = \boldsymbol{v}_i, \qquad \frac{\mathrm{d}\boldsymbol{p}_i}{\mathrm{d}t} = \boldsymbol{F}_i \tag{1}$$

where $\boldsymbol{r}_i$, $\boldsymbol{v}_i$, $\boldsymbol{p}_i = m\boldsymbol{v}_i$, and $\boldsymbol{F}_i$ are the position, velocity, momentum, and total force corresponding to bead i. The total force acting between the nonbonded beads is given as $\boldsymbol{F}_i = \sum(\boldsymbol{F}_{ij}^{\mathrm{C}} + \boldsymbol{F}_{ij}^{\mathrm{D}} + \boldsymbol{F}_{ij}^{\mathrm{R}})$, where the sum is taken over all the beads within an interaction distance r_c, which defines an intrinsic length scale of the model, and $\boldsymbol{F}_{ij}^{\mathrm{C}}$, $\boldsymbol{F}_{ij}^{\mathrm{D}}$, and $\boldsymbol{F}_{ij}^{\mathrm{R}}$ are the conservative, dissipative, and random contributions to the total force.[24,55] We use the typical soft repulsion form of the conservative force[24]

$$\boldsymbol{F}_{ij}^{\mathrm{C}} = \begin{cases} a_{ij}\left(1 - \dfrac{r_{ij}}{r_{\mathrm{c}}}\right)\boldsymbol{e}_{ij} & (r_{ij} < r_{\mathrm{c}}) \\ 0 & (r_{ij} \geq r_{\mathrm{c}}) \end{cases} \tag{2}$$

where a_{ij} is the parameter which defines the magnitude of repulsion between the beads i and j, $r_{ij} = |\boldsymbol{r}_{ij}|$ is the distance between these beads, $\boldsymbol{r}_{ij} = \boldsymbol{r}_i - \boldsymbol{r}_j$, and $\boldsymbol{e}_{ij} = \boldsymbol{r}_{ij}/r_{ij}$.

We chose $a_{ii} = 78$ (in reduced DPD units) for the interaction between the beads of the same type. This choice is based on the compressibility of water and corresponds to a coarse-graining of three water molecules into one bead.[26] The repulsion parameter for the dissimilar beads is chosen based on the affinity between these beads as[24] $a_{ij} = a_{ii} + 3.27\chi_{ij}$, where χ_{ij} is the Flory−Huggins polymer−solvent interaction parameter. The affinity of PEG beads to water beads is set by the choice of the repulsion parameter between the polymer and water beads as $a_{\mathrm{pw}} = 79.5$ based on the PEG−water Flory−Huggins interaction parameter,[15] $\chi = 0.45$. The degradable end groups are assumed to have the same solubility as a PEG monomer and hence the same interaction parameter is used for these beads.

The dissipative and random contributions to the total force are written as[24] $\boldsymbol{F}_{ij}^{\mathrm{D}} = -\gamma\omega^2(r_{ij})(\boldsymbol{e}_{ij}\cdot\boldsymbol{v}_{ij})\boldsymbol{e}_{ij}$ and $\boldsymbol{F}_{ij}^{\mathrm{R}} = \sigma\omega(r_{ij})\cdot\zeta_{ij}\cdot\Delta t^{-1/2}\boldsymbol{e}_{ij}$, correspondingly; here, γ and σ are the strengths of the dissipative and random forces, $\boldsymbol{v}_{ij} = \boldsymbol{v}_i - \boldsymbol{v}_j$ is the relative velocity, ζ_{ij} is a symmetric Gaussian distributed random variable with zero mean and unit variance, and Δt is the simulation time step. Unlike the conservative force, the dissipative and random forces are not independent but coupled to satisfy the fluctuation−dissipation theorem.[55] The strength of random force and the weight function are chosen as[24] $\sigma = 3$ and $\omega(r_{ij}) = \left(1 - \frac{r_{ij}}{r_{\mathrm{c}}}\right)$ for $r_{ij} < r_{\mathrm{c}}$ and zero otherwise. The cutoff distance r_c, temperature, and mass of a bead are set at 1.0 in reduced DPD units,[23,24] and the bead number density in the simulation box is set at 3. The simulation time step is set at $\Delta t = 0.02$. The above choice of the degree of coarse-graining results in a dimensional value of[26] $r_{\mathrm{c}} \approx 0.646$ nm. Similarly, the dimensional unit of time is obtained by relating diffusion coefficient of water beads with a known value of diffusion coefficient of water as[26] $\tau \approx 88$ ps. All quantities presented here are in reduced DPD units, with r_c as the unit length, τ as unit time, and $k_{\mathrm{B}}T$ as the unit of energy.

Bonds between the beads are introduced via the harmonic potential

$$U_{\mathrm{bond}} = \frac{K_{\mathrm{b}}}{2}(r_{ij} - r_{\mathrm{b}})^2 \tag{3}$$

where K_b is a spring constant and r_b is an equilibrium bond distance taken as[57] $K_{\mathrm{b}} = 1000$ and $r_{\mathrm{b}} = 0.7$, respectively. It is worth noting that high values of the spring constant were recently used in DPD simulations of various systems.[58−61]

The use of the mSRP[45] results in an additional force

$$F_{ij}^{\mathrm{SRP}} = b_{ij}(1 - d_{ij}/d_{\mathrm{c}})\boldsymbol{e}_{ij}^{\mathrm{S}} \tag{4}$$

acting between the centers of the bonds provided that the distance between these centers, $d_{ij} = |\boldsymbol{d}_{ij}|$, is below the cutoff distance d_c; $\boldsymbol{e}_{ij}^{\mathrm{S}} = \frac{\boldsymbol{d}_{ij}}{d_{ij}}$ in eq 4. We use $b_{ij} = 80$ and the cutoff distance $d_{\mathrm{c}} = 0.8$ in the simulations below, and these parameters were previously shown to minimize topology violations in the original framework.[45] We also conducted a series of additional simulations tracking the dynamics of entangled polymer loops to validate the effective minimization of bond crossings (see section S2 in the Supporting Information). In addition, we confirmed that with the chosen parameters, both the bond length distribution and the mean-squared internal distances for beads separated by a fixed number of bonds remain largely unaffected by the mSRP potential (see Figure S3 in the Supporting Information).

To integrate dynamic equations, the LAMMPS simulation package[62,63] with the mSRP code[45] is used. All visualizations of the hydrogel network were performed using the visual molecular dynamics software.[64] The trajectories used for the analysis below are saved every $\Delta t_{\mathrm{M}} = 5000$ time steps.

https://doi.org/10.1021/acs.jpcb.1c09570
J. Phys. Chem. B 2022, 126, 336−346

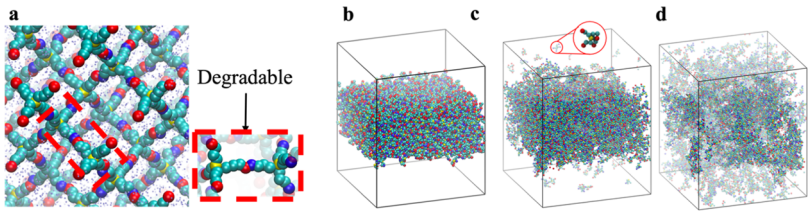

Figure 1. (a) Fragment of the polymer network with degradable bonds (bonds between red and blue beads), initial configuration prior to equilibration. Tetra-functional centers and PEG beads are shown in yellow and cyan, respectively, and water beads are shown as blue dots. (b–d) Snapshots of degradation of a reference hydrogel film (parameter set A in Table 1) with the degradation rate $k = 4.5 \times 10^{-5}$ at $t = 0$ (b), $t = 10{,}000$ (c), and $t = 20{,}000$ (d). The largest connected cluster is highlighted in each snapshot, remaining polymer beads are shown as translucent and in less saturated color. Water beads are hidden for visual clarity.

Table 1. Simulation Parameter Sets for Initial Hydrogel Films Used in This Work

parameter set	N_x	unit cell repeats	beads in one precursor	total polymer beads	tetra-arm precursors (N_0)	degradable bonds	simulation box size	total water beads
A (ref.)	6	8 × 8 × 4	13	24,960	1920	3584	42 × 42 × 50	239,640
B	6	8 × 8 × 3	13	18,304	1408	2560	42 × 42 × 50	246,296
C	6	8 × 8 × 5	13	31,616	2432	4608	42 × 42 × 60	285,904
D	6	8 × 8 × 6	13	38,272	2944	5632	42 × 42 × 70	332,168
E	10	8 × 8 × 4	21	40,320	1920	3584	57 × 57 × 60	544,500
F	14	8 × 8 × 4	29	55,680	1920	3584	66 × 66 × 60	728,400

Modeling Degradation Reaction. To simulate the bonds breaking, we use a stochastic process, similar to that used previously for various reactive systems.[38,65,66] We set the probability of bond breaking, P, and the reaction time step τ_r. Herein, we use $\tau_r = 10\Delta t$, similarly to the choice of reaction time step in previous DPD simulations of various reactive systems.[38,39,67−69] At each reaction time step a random number is generated for each degradable bond; if this number is lower than P, the bond is broken. We recently modified the mSRP framework to switch the additional forces (corresponding to the pseudo-beads) off upon bond breaking.[46] In our simulations, the time evolution of the fraction of degradable bonds intact at a given time, $p(t)$, accurately reproduces first-order degradation reaction kinetics $p = \exp(-kt)$ with the rate constant $k = P/\tau_r$; no fitting is required.[46] For a number of the polymer networks undergoing controlled photodegradation, the degradation rate constants are within the range of[2,47,51,52,70] 1 s^{-1} to 10^{-3} s^{-1}, that is, the degradation occurs orders of magnitude slower than the characteristic diffusion times on the relevant length scales.[46] Hence, low degradation rates are chosen in our simulations, ensuring that our system remains in a kinetically limited regime.[38,46]

Construction of the Initial Network Structure. The initial configuration of the tetra-PEG network is modeled as a diamond-like lattice.[38,71] The choice of diamond lattice ensures a junction functionality of four, corresponding to the network formed by the four-arm precursors. The centers of the tetra-arm precursors are placed at the lattice sites and the precursor arms are then formed by placing $N_x/2$ beads ($N_x/2 - 1$ PEG beads and one end functionality bead) along the directions from each lattice site to its nearest-neighbors. Thus, there are N_x beads between the centers of two bonded precursors. Two neighboring end functionalities are then connected, which results in an initial unit cell of the polymer network. Hydrogel films are made by replicating the polymer unit cell and are referred to as $X \times Y \times Z$, where X, Y, and Z denote the number of replicas in x, y, and z directions, respectively. The unit cell is replicated up to the simulation box faces in x and y directions with beads connected across these faces (i.e., beads at the $+x$ face are connected to the beads at the $-x$ face). In the z direction, the unit cell is replicated within the simulation box to allow space for swelling. Mere repetition (without bonding across the periodic box) of the unit cell results in precursors having a functionality less than four at the z-faces of the network. These partial precursors are deleted to yield the hydrogel film structure containing an integer number of precursors;[46] however, such deletion results in dangling polymer chains at the z-faces. Figure 1a shows a part of this initial network structure prior to the network equilibration. PEG beads and the end groups of both precursors are shown in cyan, red, and blue, respectively, and the water beads are shown as points in Figure 1a for clarity of representation. The bond between the end functionalities is set to be degradable corresponding to a cleavable site typically located in the proximity of the end functionality.[47,53] While herein we focus solely on a tetra-functional polymer network, it is worth noting that both the network connectivity and a fraction of degradable bonds can be readily tailored during the hydrogel synthesis;[48,53,72] for example, by using linear linkers of various lengths[72] or by using star-shaped precursors.[73] The corresponding variations in the network architecture prior to degradation can potentially be translated into the DPD framework in a straightforward manner by choosing different functionalities of the network junctions and specifying corresponding degradable bonds for each system of interest.

All parameters used for creating the initial polymer networks in this work are listed in Table 1. The simulation box size for films with higher N_x was increased in the horizontal direction to ensure free swelling (see Supporting Information, section S1). Additionally, the box size was increased in the z-direction for films with higher N_x or larger thickness to ensure sufficient swelling and accurate calculation of cluster sizes.

RESULTS AND DISCUSSION

Cluster Distribution and Reverse Gel Point. In the first series of simulations, we characterize the dynamics of the degradation process of the swollen network. The film is equilibrated prior to degradation as detailed in section S1 of

https://doi.org/10.1021/acs.jpcb.1c09570
J. Phys. Chem. B 2022, 126, 336−346

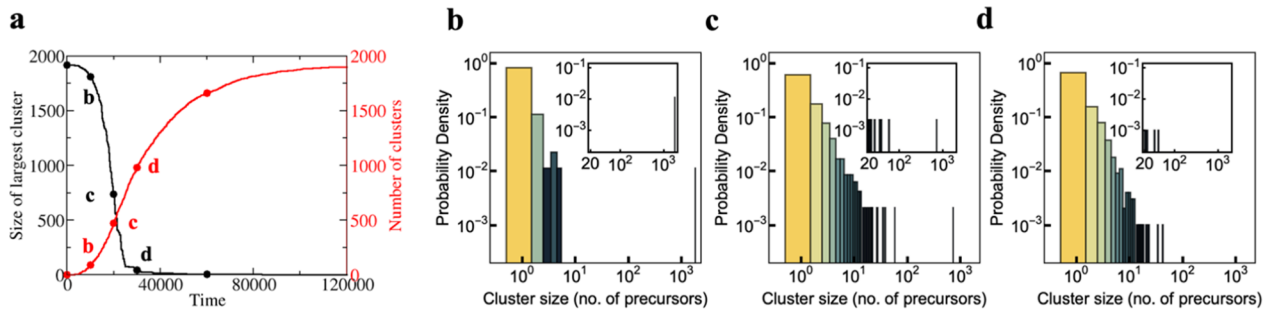

Figure 2. (a) Evolution of the size of the largest cluster (in black) and number of clusters in the system (in red) for the degradation simulation shown in figure 1. (b–d) Distribution of cluster sizes at time instants t = 10,000 (b), t = 20,000 (c), and t = 30,000 (d), and the same time instants are marked in (a). Insets in (b–d) highlight the distributions of clusters with a large number of precursors (>20 precursors).

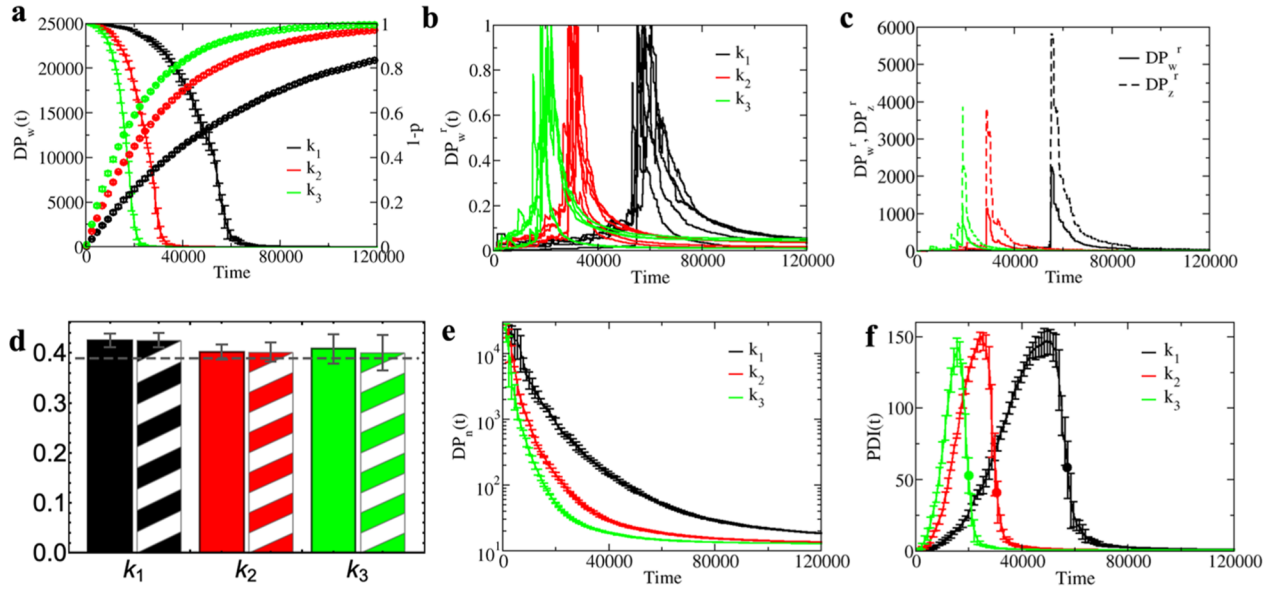

Figure 3. Time evolution of (a) weight-average degree of polymerization, DP_w (left axis) and fraction of bonds broken, $1 - p$ (right axis), (b) normalized reduced DP_w^r for five independent simulations for each degradation rate, and (c) reduced z-average degree of polymerization, DP_z^r, and DP_w^r for a single simulation run for each degradation rate. (d) Measured reverse gel points p_c^w (solid bars) and p_c^z (striped bars). Time evolution of (e) number-average degree of polymerization, DP_n, and (f) polydispersity index, PDI. Each curve in (a), (e), (f), and each data point in (d) represent average over five independent simulations, and error bars represent the standard deviation. Each curve in (b), (c) represents a single simulation, and the data in (b) are normalized by the maximum value in each simulation. Gel film with N_x = 6 and reference parameter set (set A) is considered. Black, red, and green colors in (a–f) correspond to degradation rates $k_1 = 1.5 \times 10^{-5}$, $k_2 = 3.0 \times 10^{-5}$, and $k_3 = 4.5 \times 10^{-5}$, respectively. These rates were obtained by setting $P = 3 \times 10^{-6}$, 6×10^{-6}, and 9×10^{-6} with $\tau_r = 0.2$. The degradation rate constants are provided in units of reduced simulation time, τ^{-1}.

the Supporting Information. Figure 1b shows the equilibrated hydrogel film prior to degradation. The affinity of PEG beads to water beads is chosen based on the PEG–water Flory–Huggins interaction parameter (see Methods). Snapshots in Figure 1b–d illustrate the process of degradation and erosion of the hydrogel film. After the degradation begins (e.g., after switching the light on for a photodegradable network), degradable bonds break according to the degradation rate constant, k. As a result, fragments break off from the film and are shown as translucent and in less saturated color in Figure 1c,d; water beads are not shown for clarity.

To track the degradation process, we first define a topological cluster as a group of bonded beads; correspondingly, the cluster size is defined as the number of tetra-arm precursors within the cluster. Prior to the degradation, there is a single topological cluster encompassing all the precursors within the hydrogel matrix. Evolution of both the size of the largest cluster, $N_T(t)$ (black curve, left axis), and the total number of clusters during degradation (red curve, right axis) is shown in Figure 2a. At early times, relatively small fragments leave the hydrogel, while the size of the largest cluster does not change significantly. This is evident from the simulation snapshot in Figure 1c and the corresponding distribution of cluster sizes in Figure 2b. Specifically, along with the large number of smaller fragments, only one large cluster corresponding to the degrading hydrogel film exists in the system (inset in Figure 2b). Overall, the small clusters dominate the distribution throughout the degradation process (see all distributions in Figure 2b–d). As seen in the snapshot Figure 1c, several of these small clusters leave the hydrogel film and are dispersed in the surrounding solvent, contributing to an overall mass loss.

Notably, this topological characterization does not allow us to distinguish between the smaller fragments leaving the film and the fragments that broke off but remain within the film and hence do not contribute to the mass loss. Additional

https://doi.org/10.1021/acs.jpcb.1c09570
J. Phys. Chem. B 2022, 126, 336–346

characterization needed to quantify mass loss and erosion is detailed below. As degradation proceeds, multiple larger clusters appear in the system (Figure 1d), while the size of the largest cluster sharply decreases (Figure 2a). During this sharp decrease, the percolating hydrogel network vanishes; beyond the reverse gel point, the largest cluster no longer represents the original degrading film. The existence of many relatively small clusters at late times is evident from the distributions in Figure 2c,d. Correspondingly, the largest cluster in the snapshot in Figure 1d (shown in more vivid color and seen through some of the translucent beads representing smaller clusters) is indeed relatively small and consists of only 736 precursors (or 38.33% of the total number of precursors). As degradation continues, the larger clusters disintegrate into smaller clusters and eventually into the single precursors.

To characterize the degradation process quantitatively, we carried out five independent simulations each at three different degradation rates. The averaged results from these simulations are summarized in Figure 3, where all error bars denote standard deviation over five independent simulations. To characterize reverse gelation, we use measurements similar to those that have been used to characterize gelation.[22,74−78] Accordingly, the weight-average degree of polymerization, DP_w, is defined at each moment in time as $DP_w(t) = \frac{\Sigma n_i(t) i^2}{\Sigma n_i(t) i}$, where i is the number of beads in a cluster, $n_i(t)$ is the number of clusters with i beads at time t, and summation is taken over all the clusters. The values of DP_w (Figure 3a) are high at early times corresponding to the existence of the percolating network. After an initial slow decrease, there is a sudden drop in DP_w, which is delayed at lower degradation rates because longer time is needed to break the same number of bonds.

The fraction of the bonds broken in the same systems, $1 - p(t)$, is shown on the right axis in Figure 3a; this value ranges from zero to one and represents an extent of the degradation reaction. While DP_w diverges at the gel point in analytical gelation theories,[22,77,78] it remains finite throughout simulations of finite-size systems during gelation[79] or reverse gelation. Thus, to identify the reverse gel point in our finite-size simulations, we use the reduced weight-average degree of polymerization, DP_w^r, defined as

$$DP_w^r(t) = \frac{\Sigma' n_i(t) i^2}{\Sigma' n_i(t) i} \tag{5}$$

where the summation is taken over all the clusters excluding the largest cluster.

The reduced weight-average degree of polymerization exhibits a peak at the gel point during the gelation process in finite-size systems.[74−76,80] The curves of the same color in Figure 3b correspond to five independent simulation runs for each degradation rate k and are normalized by the highest value of the DP_w^r in each independent simulation. At the initial stages of degradation, DP_w^r has a low value because the gel constitutes the only large cluster in the system. As degradation proceeds, DP_w^r exhibits a peak similar to that observed at the gel point in simulations of gelation.[74−76,81] This peak corresponds to the disintegration of the percolating network. The time instant corresponding to peaks in DP_w^r, t_c^w, allows us to identify a reverse gel point by calculating the corresponding critical value of the fraction of degradable bonds intact as

$$p_c^w = \exp(-kt_c^w) \tag{6}$$

Alternatively, reverse gel point can be identified from the analysis of the z-average degree of polymerization, $DP_z(t) = \frac{\Sigma n_i(t) i^3}{\Sigma n_i(t) i^2}$. DP_z, similar to DP_w, diverges at the gel point according to the analytical theories of gelation.[22,78] In our finite-size simulations, $DP_z(t)$ shows a behavior similar to DP_w, although it decreases slower than DP_w (Figure S4, Supporting Information). Using analogous arguments as for DP_w^r, we define the reduced z-average degree of polymerization, DP_z^r, at each time instant as

$$DP_z^r(t) = \frac{\Sigma' n_i(t) i^3}{\Sigma' n_i(t) i^2} \tag{7}$$

where the summation is taken over all the clusters excluding the largest cluster. The DP_z^r curves for one representative simulation each at the three degradation rates are plotted along with the corresponding DP_w^r curves in Figure 3c. The time corresponding to the peak in DP_z^r, t_c^z, provides a second measurement of the critical conversion at the reverse gel point $p_c^z = \exp(-kt_c^z)$. Note that the peak value of DP_z^r is higher than that of DP_w^r. The values of p_c^w and p_c^z obtained from the positions of the peaks in Figure 3b,c (averaged over five runs for each degradation rate) are provided in Figure 3d. These results show that either measurement, p_c^w or p_c^z, can be used to accurately identify the reverse gel point. An increase in standard deviation for the highest degradation rate constant can be attributed to the fact that the data are sampled for the analysis every 5000 time steps (Δt_M, see Methods) for all three cases; hence, the deviations at the higher reaction rates can potentially be reduced at the cost of increased computation time if the data are sampled more often.

Note that our measured reverse gel point is significantly higher than the value predicted by the mean-field theories for the gel point of tetra-functional networks[77,78] ($p_c = 0.33$). This could be attributed to the significant difference between the initial network structure prior to the degradation and Bethe lattice postulated in the mean-field models. The assumption of absence of any intramolecular connections used in these mean-field theories is not expected to hold for networks because existence of intramolecular connections is an essential characteristic of any network architecture.[82] Recall that the initial structure in our simulations corresponds to a diamond-like lattice. Hence, the percolation problem closest to our simulations is that of bond percolation on a diamond lattice,[83] which predicts $p_c = 0.39$ for the gelation problem (marked by the dashed line in Figure 3d). Notably, the measured reverse gel points in Figure 3d are somewhat higher than the theoretical limit of $p_c = 0.39$ corresponding to an infinite network. This could be attributed to the finite network size and is consistent with prior studies of gelation in a finite-size network, where the gel point was shown to increase with the decrease in total number of macromers forming the network with respect to the gelation point of the infinite network.[79,83]

In experiments, values close to the diamond lattice percolation problem have been observed for the gelation of tetra-arm PEG precursors near the overlap concentration,[84,85] while higher values were observed at lower concentrations. A delay in the gel point is often attributed to an increased tendency of intramolecular reactions.[80,82,86−89] Recent work by Lang and Müller[90] suggests that such an attribution may not be

https://doi.org/10.1021/acs.jpcb.1c09570
J. Phys. Chem. B 2022, 126, 336−346

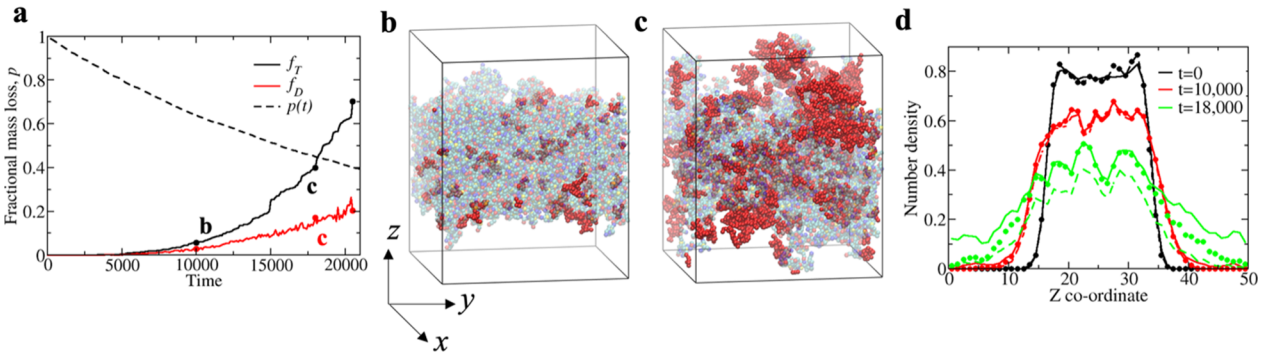

Figure 4. Characterizing mass loss from degrading network. (a) Fractional mass loss from the largest topological cluster (black curve) and the largest agglomerate (red curve) measured up to the reverse gel point (t = 20,500) for the N_x = 6, 8 × 8 × 4 hydrogel film, degradation rate is k = 4.5 × 10^{-5}. The dashed line represents the fraction of degradable bonds intact, $p(t)$, for the same simulation run. Snapshots of the degrading film at (b) t = 10,000 and (c) t = 18,000 [corresponding time instances are marked in (a)]. The fragments within the interaction distance with the largest agglomerate, including the fragments that are stuck inside the film, are highlighted in red with the rest of the polymer shown as translucent. (d) Number density distribution of all polymer beads in the vertical direction averaged over the xy plane (solid line), largest cluster (dashed line), and largest agglomerate (filled circles) at t = 0 (black), t = 10,000 (red), and t = 18,000 (green).

sufficient as the gel point delay is not fully explained by intramolecular reactions. A number of recent studies on gelation, both computational and experimental, are surveyed by Lang and Müller in the same publication.[90] In contrast to the numerous publications focusing on characterizing gelation process, analysis of the kinetics of controlled network degradation along with the measurement of reverse gel point, specifically for the systems formed by two tetra-arm precursors (often referred to as A4B4 network), is exceptionally limited. Li et al.[53] had reported a reverse gel point ranging within 0.43−0.48 for the tetra-PEG networks formed at a fixed polymer concentration but with various stoichiometric ratios. In the latter work, the authors argued that their observed reverse gel points[53] are close to the reverse gel points predicted by the site and bond percolation models on the diamond lattice. The diamond lattice model and corresponding reverse gel point have also been used by Reid et al. in their model[91] to explain experimental data of degradation behavior of tetra-arm PEG gels.

To characterize the dispersity within the degrading system, we track the number-average degree of polymerization, $\mathrm{DP}_n(t) = \frac{\Sigma n_i(t) i}{\Sigma i}$ (Figure 3e), and a polydispersity index (also referred to as dispersity), $\mathrm{PDI}(t) = \frac{\mathrm{DP}_w(t)}{\mathrm{DP}_n(t)}$ (Figure 3f), during the degradation process. Similar to DP_w, DP_n initially has a large value owing to the existence of the percolating network. As anticipated, DP_n decreases faster compared to DP_w. The PDI exhibits a peak close to the reverse gel point and decreases to one at the end of the degradation process. The peak in PDI is observed prior to the disappearance of the percolating network (average value of the reverse gel point is marked by the circle of the corresponding color in Figure 3f). The analogous trend was previously observed in simulations of gelation where the PDI peak was observed after the gel point.[80] The trend in PDI is also evident from the time evolution of the cluster size distributions in Figure 2b−d.

Fractional Mass Loss. We now turn our focus onto characterizing erosion, which can be defined as the loss of material due to the fragments leaving the original matrix.[13,18] In experiments, the fractional mass loss from the material, $f(t) = 1 - m(t)/m_0$, where m_0 is the initial mass of the material and $m(t)$ is mass of the material at a time t from the start of the degradation process, can be tracked during the degradation.[13] Unlike the apparent first-order degradation kinetics observed in experiments,[53,70,92] the fractional mass loss in experiments shows more complicated behavior, with early time slow mass loss followed by an accelerated mass loss attributed to reverse gelation.[13,20] The fast mass loss can be modeled as a discontinuity at the reverse gel point where the entire hydrogel film becomes soluble and hence complete mass loss occurs ($m(t_c) = 0$).[13]

We first measure mass loss from the largest topological cluster up to the reverse gel point by measuring the mass of topological clusters that detach from the largest cluster due to bond breaking. Because the mass of all beads is the same in DPD simulations (see Methods), we calculate a fractional mass loss as $f_T(t) = 1 - N_T(t)/N_0$ (black curve in Figure 4a, t_c = 20,500), where $N_T(t)$ is the size of the largest cluster (expressed in the number of precursors), and $N_0 = N_T(0)$ is the total number of precursors. Thus, f_T denotes the fraction of polymer beads that are no longer bonded to the hydrogel film. Two mass loss regimes can be distinguished in this fractional mass loss data. A slow mass loss regime is initially observed as only small fragments leave the hydrogel network. This slow regime occurs even though a significant fraction of degradable bonds have broken (the fraction of degradable bonds intact for the same simulation until the reverse gel point is shown in Figure 4a, dashed curve). For example, in the simulation in Figure 4a, at t = 10,000 only ≈5% of the mass is lost ($f_T(t) \approx$ 0.05) ,while ≈35% of the degradable bonds have broken [this time instant is marked by a circle (I) in Figure 4a]. In this regime, erosion primarily occurs from the surface where the tetra-arm precursors have lower connectivity to the film. Some precursors get detached but remain within the bulk of the largest cluster as discussed below. However, bonds breaking in the bulk primarily contribute to reduction in the number of elastically active polymer strands and hence to the decrease in crosslink density and corresponding swelling of the hydrogel film, as seen in Figure 1c. The initial slow mass loss from the topological largest cluster notably accelerates before the reverse gelation occurs primarily due to the detachment of larger fragments that consist of several tetra-arm precursors, as seen in Figure 1d.

The above definition of $f_T(t)$ is purely topological and does not account for spatial distribution of the clusters. Con-

https://doi.org/10.1021/acs.jpcb.1c09570
J. Phys. Chem. B 2022, 126, 336−346

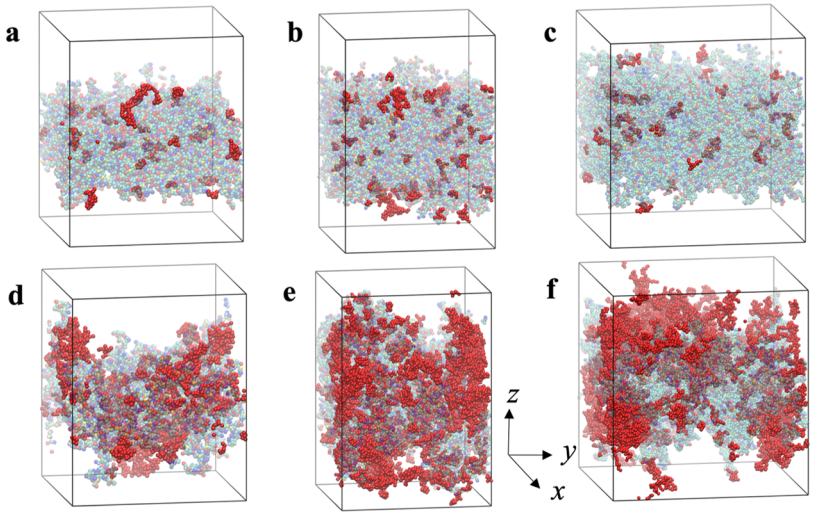

Figure 5. Snapshots of the degrading film for parameter sets B (a, d), C (b, e), and E (c, f) (see Table 1). Polymer fragments that either remain stuck within the percolated film or remain within the interaction distance from it are shown in red. Water beads and fragments that are no longer within the interaction distance with the film are hidden for clarity of representation. The beads representing the largest topological cluster are translucent. The snapshots in the top row (a–c) are taken at t = 10,000, corresponding to the fraction of degradable bonds intact p = 0.64. The snapshots in the bottom row (d–f) are taken at t = 18,000, corresponding to p = 0.44.

sequently, it does not distinguish between the broken fragments that are no longer in contact with the film and the broken fragments that remain within the bulk or within an interaction distance from the surface of the film. Hence, this definition overestimates the actual mass loss from the film. To estimate the mass loss only due to the fragments that no longer interact with the film, we define a distance-based cluster or an agglomerate as a set of beads each within r_c from at least one other bead in the agglomerate. We correspondingly introduce mass loss from the largest agglomerate as follows: $f_D(t) = 1 - N_D(t)/N_0$, where N_D is the size of the largest agglomerate (number of beads within the agglomerate normalized by the size of the precursor). The evolution of f_D for our reference case is provided in Figure 4a (red curve). The fragments that remain in the bulk or at the surface of the topological largest cluster are now incorporated into the distance-based largest cluster (or agglomerate). These fragments are highlighted in dark red and shown through the hydrogel film (the film is shown as translucent) in the snapshots at t = 10,000 (p = 0.64) and at t = 18,000 (p = 0.44) in Figure 4b,c, respectively. Note that reliable calculation of the agglomerate sizes requires that the simulation box size is large enough in the z-direction to allow space for swelling and for the detached clusters to diffuse away from the film. We chose the box size of 50 units in the z-direction because calculation of f_D for the hydrogel film with the reference parameter set is independent of the box size above this value (Figure S5 of the Supporting Information).

To characterize the spatial distribution of clusters during erosion, we compare the number density distribution of all polymer beads in the simulation box with the distribution of those beads that form the largest topological cluster and the largest agglomerate. Before any bonds are broken, the hydrogel film constitutes the largest cluster (both topological and distance-based). The number density of this equilibrated film along the z direction (averaged over xy plane) is shown in black in Figure 4d. The film thickness and spatial location prior to the degradation can be clearly identified from the black curve. As degradation begins, the film thickness increases due to swelling; this is seen in the density distributions at t = 10,000 (red curves in Figure 4d, p = 0.64). At this time instant (early stages of degradation), the differences between the density distribution of all polymer beads (solid line) and that of the largest topological cluster (dashed line) and largest agglomerate (circles) are minor. The distribution for the largest agglomerate closely follows that for all polymer beads (solid lines and circles), and the difference between the largest agglomerate and largest topological cluster is caused by the fragments highlighted in red in Figure 4b. Quantitatively, these fragments constitute only 3.15% of the mass of the largest topological cluster at t = 10,000. As the reverse gel point is approached, the relative contribution of such fragments increases to about 38.00% at t = 18,000 (p = 0.44, Figure 4c). At this later stage of the degradation, the density of the largest topological cluster within the bulk region of the film (green dashed line in Figure 4d) becomes notably lower than the density of all polymer beads and the density of the largest distance-based cluster (solid and dotted green lines, respectively). The number density distribution of the largest agglomerate matches the density distribution of all polymers in the bulk region of the film (solid and dotted green lines overlap within the bulk) but attains notably higher values than that for the largest topological cluster close to film surface due to the clusters that broke off but remain within the interaction distance. Hence, f_D defined above accounts for the largest topological cluster and the smaller topological clusters that are either stuck within the film or remain within the characteristic interaction distance. The latter contribution increases with time as the surface-to-volume ratio of the degrading cluster increases.

Effect of Sample Thickness and Crosslink Density. Having established the essential characteristics of degradation of a hydrogel film with the reference parameter set, we now turn our attention to the effects of varying physical parameters of the polymer network, specifically film thickness and crosslink density. The detailed parameters are provided in Table 1, and representative snapshots during degradation are provided in Figure 5. First, we varied the film thickness at a constant crosslink density (N_x = 6) by varying the number of

https://doi.org/10.1021/acs.jpcb.1c09570
J. Phys. Chem. B 2022, 126, 336–346

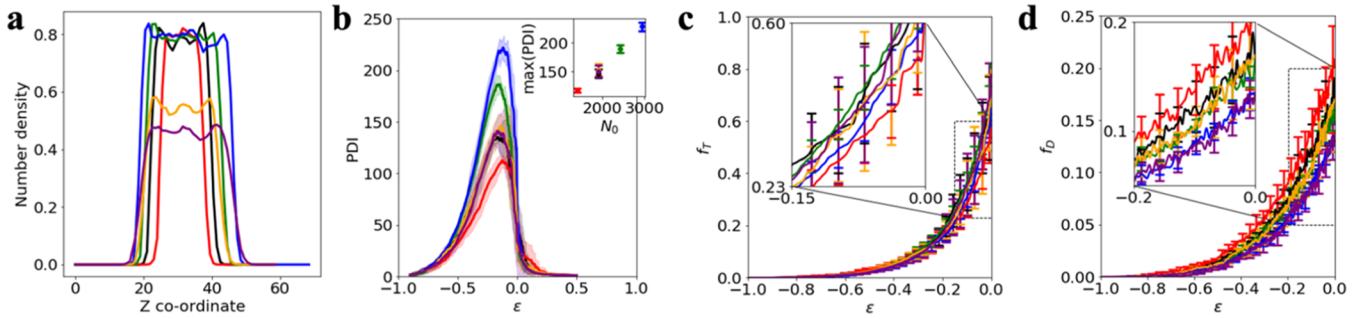

Figure 6. (a) Number density distribution of all polymer beads in the vertical direction averaged over x and y coordinates prior to degradation. (b) Polydispersity index, PDI, as a function of the relative extent of reaction, ϵ. The inset shows maximum value of PDI as a function of a number of precursors in the film, N_0. (c, d) Fractional mass loss from the largest topological cluster, f_T in (c), and from the largest agglomerate, f_D, in (d) as functions of the relative extent of reaction, ϵ. The colors in (a–d) represent simulations with the parameter sets provided in Table 1 as follows: A (black), B (red), C (green), D (blue), E (orange), and F (purple).

unit cell repetitions in the z-direction from three to six (parameter sets A–D). The thickness of the film prior to the degradation can be clearly seen from the number density plots in the z-direction averaged over the x–y plane (Figure 6a). Red, black, green, and blue curves in Figure 6 correspond to sets A through D, respectively. In the second independent series of simulations, we increased N_x, effectively decreasing the crosslink density while keeping the number of precursors fixed. This corresponds to parameter sets A (N_x = 6), E (N_x = 10), and F (N_x = 14), with corresponding data represented by black, orange, and purple curves in Figure 6. Note that such an increase in N_x also effectively increases the sample thickness prior to the degradation due to the more pronounced swelling at a lower crosslink density. Notably, the pairs of simulation parameter sets C, E and D, F are chosen to have matching thicknesses (Figure 6a) but different crosslink densities. The snapshots of the thinner and thicker films than that in the reference case during the degradation (sets B and C), and the snapshot of the sample with lower crosslink density (set E) are shown in Figure 5 (a, d), (b, e), and (c, f), respectively. These snapshots represent a relatively early stage of degradation (Figure 5a–c, top row, t = 10,000, p = 0.64) and time instant close to the reverse gel point (Figure 5d–f, bottom row, t = 18,000, p = 0.44), respectively.

We now define the relative extent of degradation reaction in analogy with the definition used to characterize the gelation process.[22] Recall that the extent of degradation reaction is $1 - p$; hence, the relative extent of reaction, ϵ, defining a proximity to the reverse gel point, can be expressed as

$$\epsilon = \frac{p_c - p}{1 - p_c} \tag{8}$$

The value of ϵ is calculated for each simulation using the corresponding calculated reverse gel point p_c ($=p_c^w$) for that simulation. ϵ increases from −1 at the onset of degradation to zero at the reverse gel point with positive values following the reverse gel point. The quantities in Figure 6b–d are plotted as a function of the proximity to the reverse gel point.

The trends in PDI discussed above (Figure 3f) hold for all cases considered. Films with the larger number of precursors show a higher peak in PDI, while an increase in N_x (an increase in the size of the precursors) has no impact on the PDI. This is anticipated because the PDI is normalized by the size of individual precursors. The maximum value of PDI is plotted as a function of the number of precursors in the inset of Figure 6b and increases approximately linearly with an increase in the number of precursors, N_0. When each PDI(ϵ) curve is normalized on N_0, all curves approximately collapse into a single master curve (Figure S6 in the Supporting Information), indicating that the polydispersity index normalized on the number of precursors depends only on the proximity to the reverse gel point.

Mass loss from the largest topological cluster, $f_T(\epsilon)$, shows the same trend for all the cases considered (Figure 6d). Large error bars in Figure 6d indicate high variability between the individual independent simulations for the same parameters; however, average trends overlap for all the parameter sets (various number and sizes of precursors). Hence, these results show that the fraction of broken-off segments, or the mass loss from the largest topological cluster, depends solely on the proximity to the reverse gel point and does not depend on the total number and size of the precursors for all the cases considered herein. For all the cases considered, the average values of f_T remain close to the apparent mass loss from the largest agglomerate, f_D, for $\epsilon \lesssim -0.65$ (Figure 6d,e).

With an increase in ϵ until the reverse gel point is reached, f_D increases significantly slower than f_T. In the proximity of the reverse gel point $\epsilon \approx 0$, the fractional mass of the broken-off fragments is more than threefold of the apparent mass loss, f_D. Furthermore, erosion from the largest agglomerate distinctly varies for some of the cases considered despite the high variability of data from individual runs (Figure 6e). The mass loss f_D close to the reverse gel point is lower for the films with larger number of precursors (green and blue curves) or lower crosslink density (orange and purple curves) compared to the reference case (black). This distinction is clear in the representative snapshots in Figures 5 and 4b,c. For the film with the reference parameter set and the film with the smaller number of precursors (Figures 4b,c and 5a,d, respectively), a significantly smaller fraction of precursors interact with the film after detachment compared to the film with more precursors (Figure 5b,e) and the film with lower crosslink density (Figure 5c,f).

To compare the effect of varying crosslink density at the same initial film thickness, we compared the pairs of simulations C, E and D, F. Both of these pairs have matching thicknesses, as seen in Figure 6a, but different N_x (N_x = 6 in sets C, D, N_x = 10 in set E, and N_x = 14 in set F). The mass loss from the largest agglomerate shows similar trends for the two simulations within each pair. This indicates that in the considered cases, the crosslink density does not significantly

https://doi.org/10.1021/acs.jpcb.1c09570
J. Phys. Chem. B 2022, 126, 336–346

affect the erosion trend, while the actual film thickness has a more pronounced effect. Finally, all the trends observed hold for three different degradation rate constants and various simulation box sizes for our reference parameter set (see section S4 in the Supporting Information). The degradation rate constant and the chosen box size did not have an impact on the mass loss from the largest agglomerate, indicating that the detached fragments have sufficient space and time to diffuse away from the largest agglomerate. However, a significant fraction of these fragments remains within or in the close proximity of the largest cluster representing a degrading film near the reverse gel point.

CONCLUSIONS

Herein, we utilized DPD simulations to capture degradation and erosion of polymer networks on the mesoscale. We characterized the degradation process via tracking the time evolution of distribution of broken-off fragments. The reverse gel point corresponding to the disappearance of the percolated network was calculated using the reduced weight-average and z-average degrees of polymerization. We then used this calculated reverse gel point to define the relative extent of reaction which identifies the proximity to the reverse gel point. We demonstrated that the fraction of broken-off fragments depends solely on the relative extent of the reaction for the samples with various number of precursors, different film thicknesses, and different crosslink densities prior to the degradation. We showed that the polydispersity index exhibits a distinct peak prior to the disappearance of the percolating network and strongly decreases at the reverse gel point. The observed peak in PDI scales approximately linearly with the number of precursors; furthermore, the PDI normalized on the total number of precursors depends primarily on the proximity to the reverse gel point.

The reverse gel point measured in our simulations is comparable to predictions of bond percolation theory on a diamond lattice.[83] Small positive deviations from the analytical value seen in our measurements are likely due to the relatively small number of precursors.[79] This analytical value also describes the experimentally measured values of both the gel point[84,85] and reverse gel point[53] of networks formed with tetra-arm precursors. Notably, the measured value of the reverse gel point is significantly higher than the value predicted by the mean-field theories for the gel point of tetra-functional networks.[77,78] This is attributed to the fact that the assumption of absence of any intramolecular connections used in these mean-field theories is not expected to hold for a network[82] prior to degradation. Relatively high reverse gel point observed herein is consistent with the delay of the gel point during the gelation process in the presence of the finite-size loops.[79]

Furthermore, we characterized the erosion from the swollen polymer network via tracking the apparent mass loss that accounts for the fragments remaining stuck within or in contact with the percolated network (f_D). We showed that while this apparent mass loss remains approximately the same as mass loss from the largest topological cluster for low relative extent of reaction ($\epsilon \lesssim -0.65$), an increase in ϵ until the reverse gel point is reached results in significantly slower increase in f_D than f_T. In the proximity of the reverse gel point, the fractional mass of the broken-off fragments is more than threefold of the apparent mass loss, f_D. Furthermore, we quantified that the erosion process from the largest agglomerate does not solely depend on the relative extent of reaction but also distinctly varies with the physical properties of the gel such as sample thickness. Hence, both characteristics, f_D and f_T, are necessary to quantify and predict the outcome of the erosion process. These results elucidate the main features of degradation and erosion on the mesoscale and could provide guidelines for designing degrading materials with controlled properties.

ASSOCIATED CONTENT

Supporting Information

The Supporting Information is available free of charge at https://pubs.acs.org/doi/10.1021/acs.jpcb.1c09570.

Additional simulation details, verification of effective minimization of topology violations, time evolution of weight-average and z-average degrees of polymerization during degradation, effects of box size and degradation rate constant on cluster size calculation, and polydispersity index normalized by the total number of precursors versus relative extent of reaction (PDF)

AUTHOR INFORMATION

Corresponding Author

Olga Kuksenok − *Department of Materials Science and Engineering, Clemson University, Clemson, South Carolina 29634, United States;* orcid.org/0000-0002-1895-5206; Email: okuksen@clemson.edu

Author

Vaibhav Palkar − *Department of Materials Science and Engineering, Clemson University, Clemson, South Carolina 29634, United States;* orcid.org/0000-0002-8192-0399

Complete contact information is available at: https://pubs.acs.org/10.1021/acs.jpcb.1c09570

Notes

The authors declare no competing financial interest.

ACKNOWLEDGMENTS

The authors thank Chandan K. Choudhury and Ulf D. Schiller for valuable discussions. This work was supported in part by the National Science Foundation EPSCoR Program under NSF award no. OIA-1655740. Any opinions, findings, and conclusions or recommendations expressed in this material are those of the author(s) and do not necessarily reflect those of the National Science Foundation. Clemson University is acknowledged for generous allotment of compute time on Palmetto cluster.

REFERENCES

(1) Shieh, P.; Zhang, W.; Husted, K. E. L.; Kristufek, S. L.; Xiong, B.; Lundberg, D. J.; Lem, J.; Veysset, D.; Sun, Y.; Nelson, K. A.; et al. Cleavable comonomers enable degradable, recyclable thermoset plastics. *Nature* **2020**, *583*, 542−547.

(2) LeValley, P. J.; Neelarapu, R.; Sutherland, B. P.; Dasgupta, S.; Kloxin, C. J.; Kloxin, A. M. Photolabile Linkers: Exploiting Labile Bond Chemistry to Control Mode and Rate of Hydrogel Degradation and Protein Release. *J. Am. Chem. Soc.* **2020**, *142*, 4671−4679.

(3) Lin, C.-C.; Anseth, K. S. PEG Hydrogels for the Controlled Release of Biomolecules in Regenerative Medicine. *Pharm. Res.* **2009**, *26*, 631−643.

(4) Azagarsamy, M. A.; Alge, D. L.; Radhakrishnan, S. J.; Tibbitt, M. W.; Anseth, K. S. Photocontrolled Nanoparticles for On-Demand Release of Proteins. *Biomacromolecules* **2012**, *13*, 2219−2224.

(5) McKinnon, D. D.; Brown, T. E.; Kyburz, K. A.; Kiyotake, E.; Anseth, K. S. Design and Characterization of a Synthetically Accessible, Photodegradable Hydrogel for User-Directed Formation of Neural Networks. *Biomacromolecules* **2014**, *15*, 2808−2816.
(6) Kloxin, A. M.; Kasko, A. M.; Salinas, C. N.; Anseth, K. S. Photodegradable Hydrogels for Dynamic Tuning of Physical and Chemical Properties. *Science* **2009**, *324*, 59−63.
(7) Frey, M. T.; Wang, Y.-l. A photo-modulatable material for probing cellular responses to substrate rigidity. *Soft Matter* **2009**, *5*, 1918−1924.
(8) Wong, D. Y.; Griffin, D. R.; Reed, J.; Kasko, A. M. Photodegradable Hydrogels to Generate Positive and Negative Features over Multiple Length Scales. *Macromolecules* **2010**, *43*, 2824−2831.
(9) Luo, Y.; Shoichet, M. S. A photolabile hydrogel for guided three-dimensional cell growth and migration. *Nat. Mater.* **2004**, *3*, 249−253.
(10) Griffin, D. R.; Kasko, A. M. Photoselective Delivery of Model Therapeutics from Hydrogels. *ACS Macro Lett.* **2012**, *1*, 1330−1334.
(11) Ramanan, V. V.; Katz, J. S.; Guvendiren, M.; Cohen, E. R.; Marklein, R. A.; Burdick, J. A. Photocleavable side groups to spatially alter hydrogel properties and cellular interactions. *J. Mater. Chem.* **2010**, *20*, 8920−8926.
(12) Kloxin, A. M.; Tibbitt, M. W.; Kasko, A. M.; Fairbairn, J. A.; Anseth, K. S. Tunable Hydrogels for External Manipulation of Cellular Microenvironments through Controlled Photodegradation. *Adv. Mater.* **2010**, *22*, 61.
(13) Metters, A. T.; Bowman, C. N.; Anseth, K. S. A statistical kinetic model for the bulk degradation of PLA-b-PEG-b-PLA hydrogel networks. *J. Phys. Chem. B* **2000**, *104*, 7043−7049.
(14) Jahanmir, G.; Abdekhodaie, M. J.; Chau, Y. Stochastic Modeling of Degradation Behavior of Hydrogels. *Macromolecules* **2018**, *51*, 3941−3952.
(15) Metters, A.; Hubbell, J. Network formation and degradation behavior of hydrogels formed by Michael-type addition reactions. *Biomacromolecules* **2005**, *6*, 290−301.
(16) Reddy, S. K.; Anseth, K. S.; Bowman, C. N. Modeling of network degradation in mixed step-chain growth polymerizations. *Polymer* **2005**, *46*, 4212−4222.
(17) Tibbitt, M. W.; Kloxin, A. M.; Anseth, K. S. Modeling controlled photodegradation in optically thick hydrogels. *J. Polym. Sci., Polym. Chem.* **2013**, *51*, 1899−1911.
(18) Göpferich, A. Polymer Bulk Erosion. *Macromolecules* **1997**, *30*, 2598−2604.
(19) Lalitha Sridhar, S.; Schneider, M. C.; Chu, S.; de Roucy, G.; Bryant, S. J.; Vernerey, F. J. Heterogeneity is key to hydrogel-based cartilage tissue regeneration. *Soft Matter* **2017**, *13*, 4841−4855.
(20) Ashley, G. W.; Henise, J.; Reid, R.; Santi, D. V. Hydrogel drug delivery system with predictable and tunable drug release and degradation rates. *Proc. Natl. Acad. Sci. U. S. A.* **2013**, *110*, 2318−2323.
(21) Shih, H.; Lin, C.-C. Cross-Linking and Degradation of Step-Growth Hydrogels Formed by Thiol-Ene Photoclick Chemistry. *Biomacromolecules* **2012**, *13*, 2003−2012.
(22) Rubinstein, M.; Colby, R. H. *Polymer Physics*; OUP: Oxford, 2003.
(23) Hoogerbrugge, P. J.; Koelman, J. M. V. A. Simulating Microscopic Hydrodynamic Phenomena with Dissipative Particle Dynamics. *Europhys. Lett.* **1992**, *19*, 155−160.
(24) Groot, R. D.; Warren, P. B. Dissipative particle dynamics: Bridging the gap between atomistic and mesoscopic simulation. *J. Chem. Phys.* **1997**, *107*, 4423−4435.
(25) Español, P.; Warren, P. B. Perspective: Dissipative Particle Dynamics. *J. Chem. Phys.* **2017**, *146*, 150901.
(26) Groot, R. D.; Rabone, K. L. Mesoscopic Simulation of Cell Membrane Damage, Morphology Change and Rupture by Nonionic Surfactants. *Biophys. J.* **2001**, *81*, 725−736.
(27) Feng, Y. H.; Zhang, X. P.; Zhao, Z. Q.; Guo, X. D. Dissipative Particle Dynamics Aided Design of Drug Delivery Systems: A Review. *Mol. Pharm.* **2020**, *17*, 1778−1799.
(28) Wang, X.; Santo, K. P.; Neimark, A. V. Modeling Gas-Liquid Interfaces by Dissipative Particle Dynamics: Adsorption and Surface Tension of Cetyl Trimethyl Ammonium Bromide at the Air-Water Interface. *Langmuir* **2020**, *36*, 14686−14698.
(29) Santo, K. P.; Neimark, A. V. Effects of metal-polymer complexation on structure and transport properties of metal-substituted polyelectrolyte membranes. *J. Colloid Interface Sci.* **2021**, *602*, 654−668.
(30) Salib, I.; Yong, X.; Crabb, E. J.; Moellers, N. M.; McFarlin, G. T.; Kuksenok, O.; Balazs, A. C. Harnessing Fluid-Driven Vesicles To Pick Up and Drop Off Janus Particles. *ACS Nano* **2013**, *7*, 1224−1238.
(31) Dutt, M.; Kuksenok, O.; Nayhouse, M. J.; Little, S. R.; Balazs, A. C. Modeling the Self-Assembly of Lipids and Nanotubes in Solution: Forming Vesicles and Bicelles with Transmembrane Nanotube Channels. *ACS Nano* **2011**, *5*, 4769−4782.
(32) Shin, J. M.; Kim, Y.; Yun, H.; Yi, G.-R.; Kim, B. J. Morphological Evolution of Block Copolymer Particles: Effect of Solvent Evaporation Rate on Particle Shape and Morphology. *ACS Nano* **2017**, *11*, 2133−2142.
(33) Vishnyakov, A.; Lee, M.-T.; Neimark, A. V. Prediction of the Critical Micelle Concentration of Nonionic Surfactants by Dissipative Particle Dynamics Simulations. *J. Phys. Chem. Lett.* **2013**, *4*, 797−802.
(34) Mills, Z. G.; Mao, W.; Alexeev, A. Mesoscale modeling: solving complex flows in biology and biotechnology. *Trends Biotechnol.* **2013**, *31*, 426−434.
(35) Chen, S.; Yong, X. Dissipative particle dynamics modeling of hydrogel swelling by osmotic ensemble method. *J. Chem. Phys.* **2018**, *149*, 094904.
(36) Nikolov, S.; Fernandez-Nieves, A.; Alexeev, A. Mesoscale modeling of microgel mechanics and kinetics through the swelling transition. *Appl. Math. Mech.* **2018**, *39*, 47−62.
(37) Gumerov, R. A.; Filippov, S. A.; Richtering, W.; Pich, A.; Potemkin, I. I. Amphiphilic microgels adsorbed at oil-water interfaces as mixers of two immiscible liquids. *Soft Matter* **2019**, *15*, 3978−3986.
(38) Yong, X.; Kuksenok, O.; Matyjaszewski, K.; Balazs, A. C. Harnessing Interfacially-Active Nanorods to Regenerate Severed Polymer Gels. *Nano Lett.* **2013**, *13*, 6269−6274.
(39) Singh, A.; Kuksenok, O.; Johnson, J. A.; Balazs, A. C. Tailoring the structure of polymer networks with iniferter-mediated photo-growth. *Polym. Chem.* **2016**, *7*, 2955−2964.
(40) Choudhury, C. K.; Palkar, V.; Kuksenok, O. Computational Design of Nanostructured Soft Interfaces: Focus on Shape Changes and Spreading of Cubic Nanogels. *Langmuir* **2020**, *36*, 7109−7123.
(41) Yong, X.; Simakova, A.; Averick, S.; Gutierrez, J.; Kuksenok, O.; Balazs, A. C.; Matyjaszewski, K. Stackable, Covalently Fused Gels: Repair and Composite Formation. *Macromolecules* **2015**, *48*, 1169−1178.
(42) Chen, S.; Yong, X. Elastocapillary interactions of thermoresponsive microgels across the volume phase transition temperatures. *J. Colloid Interface Sci.* **2021**, *584*, 275−280.
(43) Nikolov, S. V.; Fernandez-Nieves, A.; Alexeev, A. Behavior and mechanics of dense microgel suspensions. *Proc. Natl. Acad. Sci. U. S. A.* **2020**, *117*, 27096−27103.
(44) Anakhov, M. V.; Gumerov, R. A.; Potemkin, I. I. Stimuli-responsive aqueous microgels: properties and applications. *Mendeleev Commun.* **2020**, *30*, 555−562.
(45) Sirk, T. W.; Slizoberg, Y. R.; Brennan, J. K.; Lisal, M.; Andzelm, J. W. An enhanced entangled polymer model for dissipative particle dynamics. *J. Chem. Phys.* **2012**, *136*, 134903.
(46) Palkar, V.; Choudhury, C. K.; Kuksenok, O. Development of Dissipative Particle Dynamics framework for modeling hydrogels with degradable bonds. *MRS Adv.* **2020**, *5*, 927−934.
(47) Azagarsamy, M. A.; McKinnon, D. D.; Alge, D. L.; Anseth, K. S. Coumarin-Based Photodegradable Hydrogel: Design, Synthesis, Gelation, and Degradation Kinetics. *ACS Macro Lett.* **2014**, *3*, 515−519.
(48) Madl, C. M.; Katz, L. M.; Heilshorn, S. C. Tuning Bulk Hydrogel Degradation by Simultaneous Control of Proteolytic

Cleavage Kinetics and Hydrogel Network Architecture. *ACS Macro Lett.* **2018**, *7*, 1302−1307.
(49) Sakai, T.; Matsunaga, T.; Yamamoto, Y.; Ito, C.; Yoshida, R.; Suzuki, S.; Sasaki, N.; Shibayama, M.; Chung, U.-i. Design and fabrication of a high-strength hydrogel with ideally homogeneous network structure from tetrahedron-like macromonomers. *Macromolecules* **2008**, *41*, 5379−5384.
(50) Richtering, W.; Saunders, B. R. Gel architectures and their complexity. *Soft Matter* **2014**, *10*, 3695−3702.
(51) Truong, V. X.; Li, F.; Forsythe, J. S. Photolabile Hydrogels Responsive to Broad Spectrum Visible Light for Selective Cell Release. *ACS Appl. Mater. Interfaces* **2017**, *9*, 32441−32445.
(52) Villiou, M.; Paez, J. I.; del Campo, A. Photodegradable Hydrogels for Cell Encapsulation and Tissue Adhesion. *ACS Appl. Mater. Interfaces* **2020**, *12*, 37862−37872.
(53) Li, X.; Tsutsui, Y.; Matsunaga, T.; Shibayama, M.; Chung, U.-i.; Sakai, T. Precise Control and Prediction of Hydrogel Degradation Behavior. *Macromolecules* **2011**, *44*, 3567−3571.
(54) Hoogerbrugge, P. J.; Koelman, J. M. V. A. Simulating microscopic hydrodynamic phenomena with dissipative particle dynamics. *Europhys. Lett.* **1992**, *19*, 155−160.
(55) Español, P. Statistical Mechanics of Dissipative Particle Dynamics. *Europhys. Lett.* **1995**, *30*, 191.
(56) Santo, K. P.; Neimark, A. V. Dissipative particle dynamics simulations in colloid and interface science: A review. *Adv. Colloid Interface Sci.* **2021**, *298*, 102545.
(57) Choudhury, C. K.; Palkar, V.; Kuksenok, O. Computational design of nanostructured soft interfaces: focus on shape changes and spreading of cubic nanogels. *Langmuir* **2020**, *36*, 7109.
(58) Vishnyakov, A.; Mao, R.; Lee, M.-T.; Neimark, A. V. Coarse-grained model of nanoscale segregation, water diffusion, and proton transport in Nafion membranes. *J. Chem. Phys.* **2018**, *148*, 024108.
(59) Bray, D. J.; Anderson, R. L.; Warren, P. B.; Lewtas, K. Wax Formation in Linear and Branched Alkanes with Dissipative Particle Dynamics. *J. Chem. Theory Comput.* **2020**, *16*, 7109.
(60) Choudhury, C. K.; Kuksenok, O. Native-Based Dissipative Particle Dynamics Approach for α-Helical Folding. *J. Phys. Chem. B* **2020**, *124*, 11379−11386.
(61) Choudhury, C. K.; Kuksenok, O. Modeling dynamics of Polyacrylamide Gel in Oil-Water Mixtures: Dissipative Particle Dynamics Approach. *MRS Adv.* **2018**, *3*, 1469−1474.
(62) Plimpton, S. Fast Parallel Algorithms for Short-Range Molecular Dynamics. *J. Comput. Phys.* **1995**, *117*, 1−19.
(63) LAMMPS molecular dynamics simulator. http://lammps.sandia.gov (accessed Dec 12, 2021).
(64) Humphrey, W.; Dalke, A.; Schulten, K. VMD: Visual molecular dynamics. *J. Mol. Graphics Modell.* **1996**, *14*, 33−38.
(65) Akkermans, R. L. C.; Toxvaerd, S. r.; Briels, W. J. Molecular dynamics of polymer growth. *J. Chem. Phys.* **1998**, *109*, 2929−2940.
(66) Milchev, A.; Wittmer, J. P.; Landau, D. P. Formation and equilibrium properties of living polymer brushes. *J. Chem. Phys.* **2000**, *112*, 1606−1615.
(67) Liu, H.; Li, M.; Lu, Z.-Y.; Zhang, Z.-G.; Sun, C.-C. Influence of Surface-Initiated Polymerization Rate and Initiator Density on the Properties of Polymer Brushes. *Macromolecules* **2009**, *42*, 2863−2872.
(68) Yong, X.; Kuksenok, O.; Balazs, A. C. Modeling free radical polymerization using dissipative particle dynamics. *Polymer* **2015**, *72*, 217−225.
(69) Singh, A.; Kuksenok, O.; Johnson, J. A.; Balazs, A. C. Photo-regeneration of severed gel with iniferter-mediated photo-growth. *Soft Matter* **2017**, *13*, 1978−1987.
(70) Brown, T. E.; Marozas, I. A.; Anseth, K. S. Amplified Photodegradation of Cell-Laden Hydrogels via an Addition-Fragmentation Chain Transfer Reaction. *Adv. Mater.* **2017**, *29*, 1605001.
(71) Jha, P. K.; Zwanikken, J. W.; Detcheverry, F. A.; De Pablo, J. J.; Olvera de la Cruz, M. Study of volume phase transitions in polymeric nanogels by theoretically informed coarse-grained simulations. *Soft Matter* **2011**, *7*, 5965−5975.
(72) Schultz, K. M.; Anseth, K. S. Monitoring degradation of matrix metalloproteinases-cleavable PEG hydrogels via multiple particle tracking microrheology. *Soft Matter* **2013**, *9*, 1570−1579.
(73) Krüger, A. J. D.; Köhler, J.; Cichosz, S.; Rose, J. C.; Gehlen, D. B.; Haraszti, T.; Möller, M.; De Laporte, L. A catalyst-free, temperature controlled gelation system for in-mold fabrication of microgels. *Chem. Commun.* **2018**, *54*, 6943−6946.
(74) Gupta, A. M.; Hendrickson, R. C.; Macosko, C. W. Monte Carlo description of Af homopolymerization: Diffusional effects. *J. Chem. Phys.* **1991**, *95*, 2097−2108.
(75) Shy, L. Y.; Leung, Y. K.; Eichinger, B. E. Critical exponents for off-lattice gelation of polymer chains. *Macromolecules* **1985**, *18*, 983−986.
(76) Šomvársky, J.; Dušek, K. Kinetic Monte-Carlo simulation of network formation. *Polym. Bull.* **1994**, *33*, 377−384.
(77) Flory, P. J. Molecular Size Distribution in Three Dimensional Polymers. I. Gelation1. *J. Am. Chem. Soc.* **1941**, *63*, 3083−3090.
(78) Macosko, C. W.; Miller, D. R. A New Derivation of Average Molecular Weights of Nonlinear Polymers. *Macromolecules* **1976**, *9*, 199−206.
(79) Lin, T.-S.; Wang, R.; Johnson, J. A.; Olsen, B. D. Topological Structure of Networks Formed from Symmetric Four-Arm Precursors. *Macromolecules* **2018**, *51*, 1224−1231.
(80) Polanowski, P.; Jeszka, J. K.; Li, W.; Matyjaszewski, K. Effect of dilution on branching and gelation in living copolymerization of monomer and divinyl cross-linker: Modeling using dynamic lattice liquid model (DLL) and Flory-Stockmayer (FS) model. *Polymer* **2011**, *52*, 5092−5101.
(81) Polanowski, P.; Jeszka, J. K.; Matyjaszewski, K. Modeling of branching and gelation in living copolymerization of monomer and divinyl cross-linker using dynamic lattice liquid model (DLL) and Flory-Stockmayer model. *Polymer* **2010**, *51*, 6084−6092.
(82) Flory, P. J. *Principles of Polymer Chemistry*; Cornell University Press, 1953.
(83) Stauffer, D.; Aharony, A. *Introduction to Percolation Theory*; Taylor & Francis, 1994.
(84) Sakai, T.; Katashima, T.; Matsushita, T.; Chung, U.-i. Sol-gel transition behavior near critical concentration and connectivity. *Polym. J.* **2016**, *48*, 629−634.
(85) Nishi, K.; Fujii, K.; Chung, U.-i.; Shibayama, M.; Sakai, T. Experimental Observation of Two Features Unexpected from the Classical Theories of Rubber Elasticity. *Phys. Rev. Lett.* **2017**, *119*, 267801.
(86) Rankin, S. E.; Kasehagen, L. J.; McCormick, A. V.; Macosko, C. W. Dynamic Monte Carlo simulation of gelation with extensive cyclization. *Macromolecules* **2000**, *33*, 7639−7648.
(87) Spouge, J. L. Equilibrium ring formation in polymer solutions. *J. Stat. Phys.* **1986**, *43*, 143−196.
(88) Wang, R.; Lin, T.-S.; Johnson, J. A.; Olsen, B. D. Kinetic Monte Carlo Simulation for Quantification of the Gel Point of Polymer Networks. *ACS Macro Lett.* **2017**, *6*, 1414−1419.
(89) Tanaka, Y.; Stanford, J. L.; Stepto, R. Interpretation of Gel Points of an Epoxy-Amine System Including Ring Formation and Unequal Reactivity: Measurements of Gel Points and Analyses on Ring Structures. *Macromolecules* **2012**, *45*, 7197−7205.
(90) Lang, M.; Müller, T. Analysis of the Gel Point of Polymer Model Networks by Computer Simulations. *Macromolecules* **2020**, *53*, 498−512.
(91) Reid, R.; Sgobba, M.; Raveh, B.; Rastelli, G.; Sali, A.; Santi, D. V. Analytical and Simulation-Based Models for Drug Release and Gel-Degradation in a Tetra-PEG Hydrogel Drug-Delivery System. *Macromolecules* **2015**, *48*, 7359−7369.
(92) Lin, C.-C.; Metters, A. T. Hydrogels in controlled release formulations: Network design and mathematical modeling. *Adv. Drug Delivery Rev.* **2006**, *58*, 1379−1408.

https://doi.org/10.1021/acs.jpcb.1c09570
J. Phys. Chem. B 2022, 126, 336−346